Mechanism of biomimetic virus-like nanoparticles in triggering immune response elucidated by proteomics

Jiajia Wang[1], Ahmed Montaser[2], Minna Sivonen[1], Henri Leinonen[2], Jussi Hepojoki [3], Vesa-Pekka Lehto[1], and Wujun Xu[1*]

[1]*Department of Technical Physics, University of Eastern Finland, Kuopio, 70211, Finland*

[2]*School of Pharmacy, University of Eastern Finland, Kuopio, 70211, Finland*

[3]*Department of Virology, University of Helsinki, Helsinki, 00014, Finland*

[*]Corresponding authors: wujun.xu@uef.fi

Abstract

Biomimetic nanoparticles (NPs) with virus-like shapes have been developed as novel delivery platforms and immune adjuvants to enhance immune response. However, the interaction mechanism between the nanoparticles and immune cells has been poorly understood. Hence, virus-like mesoporous silica nanoparticles (VLP) were developed and characterized with several physicochemical methods in the present study. The VLP showed an increased cellular uptake and enhanced immune response due to its biomimetic spikes on the surface compared to spherical NPs. Proteomic analysis revealed that the RIG-I-like receptor, chemokine, MAPK, Toll-like receptor signaling, and Th1 and Th2 cell differentiation pathways were involved in regulating the immune response when macrophages interacted with VLP. When the spikes increased from 5 to 30 nm, the expression levels of immune-related proteins including TRAF6 and PIAS4 proteins enhanced. This study revealed the interaction pathways and key proteins in the activation of immune response with VLP, which may provide insights to develop novel immunotherapy for enhanced efficacy.

Key words: Virus like nanoparticles, Mesoporous silica nanoparticles, Immunotherapy, Proteomics,

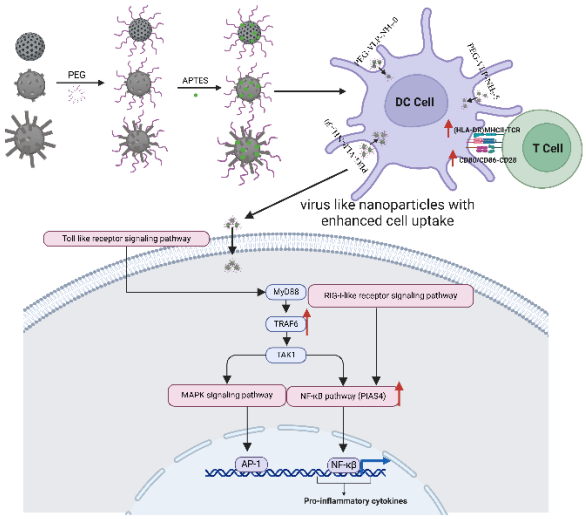

Introduction

Mesoporous silica nanoparticles (MSNs) have gained significant attention in cancer therapy due to their unique properties, such as uniform mesoporous structure, large surface area, good biocompatibility, high loading capacity, and easy functionalization[1,2]. For cancer immunotherapy, MSNs have been explored as immune adjuvants to stimulate both innate and adaptive immune responses[3]. In addition, due to their high surface area, and they are good nanocarriers to deliver different therapeutic antigens for cancer vaccines[4]. For example, MSNs enhanced the intracellular delivery of R848, a Toll-like receptor agonist into the lysosomes of antigen-presenting cells (APCs), thus dendritic cells (DCs) and antigen-specific T cell responses were effectively activated[5]. Furthermore, MSNs have outstanding performance in the co-delivery of multiple agents and sustained antigen release, which may lead to synergistic interaction and stimulate durable effective cytotoxic T lymphocyte (CTL) responses against tumors[6].

It remains a critical challenge to improve the efficiency of cellular internalization for enhancing the therapeutic potential because cells have complex membranes and defense mechanisms that limit the uptake of foreign substances, including therapeutic agents[7]. Inspired by pathogens[8,9], researchers have designed virus-like nanomaterials with biomimetic topological structures for immunotherapy[10]. The morphology of nanoparticles (NP) has a significant impact on cell membrane binding and instability. Sara Malekkhaiat Häffner et al found that the spikes on the surface of virus-like mesoporous silica (VLP)

particles can disrupt the lipid bilayer of cell membranes[11] and thus the VLP naturally possess enhanced cellular uptake. For example, Gao et al showed VLP mimic viral structures to enhance antigen delivery and immune activation. Co-loaded with imiquimod (IMQ) and ovalbumin (OVA), VLPs can improve cellular uptake and activate CD8+ T cells, effectively inhibit B16-OVA tumor growth and advance nonvaccine strategies for cancer immunotherapy. VLPs have superior biocompatibility in both cellular and in vivo models, enhanced cellular uptake, and a unique endocytic pathway that facilitated lysosomal escape and promoted antigen cross-presentation[12,13]. Though several types of Nano vaccines have been investigated in cancer immunotherapy, the mechanism of the VLPs in activating immune responses remain poorly understood.

Proteomics is a powerful tool for the large-scale study of proteins for understanding biological processes and disease therapy mechanisms[14]. It has been widely used in nanomedicine to identify protein corona formed on NPs and protein biomarkers for targeted drug delivery[15,16]. Since changes in protein expression are a key characteristic of immunotherapy, proteomics is also utilized to examine the immune interactions between cells and NPs. For example, Véronique Collin-Faure showed that the effects of polystyrene particles of varying sizes on macrophage polarization and inflammatory responses, the key proteins such as leupaxin or Pycard, under the innate immunit pathway from proteomic data were analyzed to explore the impact on immune responses[17].

The aim of the present study is to verify the activation of immune response with VLP NPs and further discover the mechanism with proteomics analysis. The VLPs were prepared via microemulsion growth method[12] and then functionalized with Polyethylene glycol (PEG) and amine silane. The NPs were characterized by transmission electron microscopy (TEM), thermogravimetric analysis (TGA), and zeta potential measurements. The cytotoxicity, internalization efficiency, and immune response activation of the NPs were evaluated using cell viability assays, fluorescence microscopy, and flow cytometry, respectively. Finally, the immune response mechanism was studied with proteomics. Pathway enrichment was conducted, including pathway heatmaps from immunological databases, to identify immune-related pathways. Protein interaction networks and spike-dependent protein expression heatmaps were further

analyzed. The present study may promote the fundamental understanding of the immune response triggered by VLPs, which offers new perspectives and directions to develop more efficient cancer immunotherapy.

Materials and methods

Preparation of the virus-like silica nanoparticles

Hexadecyltrimethylammonium bromide (CTAB, Sigma) was dissolved in deionized water with the concentration of 1%. 0.1 M sodium hydroxide was added slowly into the solution. The solution was stirred in an oil bath at 60 °C. Then, the mixture of tetraethyl orthosilicate (TEOS, Merck) and cyclohexane (Merck) with volume ratio=1:4 was added. The length of spikes on the VLP was controlled by adjusting reaction. The reaction mixture was stirred for 20, 48, and 70 hours to prepare the VLP with the spike length of 0, 5 and 30 nm respectively. After the reaction, the VLP was washed twice with ethanol to remove unreacted chemicals. And then, the VLP were refluxed in a mixture of 150 ml ethanol at 99 °C for 48 hours to remove the surfactant template. The NPs were stored in the ethanol at ambient temperature for further use.

To modify the VLP with PEG, 2-[Methoxy(polyethyleneoxy)propyl] trimethoxy silane (90%, 6-9 PEG-units, abcr) was mixed with VLP in ethanol and heated to 90 °C with an oil bath. After stirring for 30 minutes, the NPs were washed twice with ethanol. 3-Aminopropyltriethoxysilane (APTES, VWR) was mixed with the PEG-modified VLP and stirred at 65 °C for 1 hour, then washed with ethanol to remove unreacted chemicals. The samples were named PEG-VLP-NH_2-0, PEG-VLP-NH_2-5, and PEG-VLP-NH_2-30, corresponding to the NPs with the spike length of 0, 5, 30 nm, respectively.

Characterization of VLP

The particle morphology was characterized by using transmission electron microscopy (TEM). Diluted suspensions of VLP were dropped onto carbon film grids (HC400-Cu, USA), dried in room temperature, and imaged using Jeol JEM-2100F TEM. The plain VLPs and after modified VLPs were measured by using Zetasizer Nano ZS (Malvern Panalytical Ltd, United Kingdom). Thermogravimetric analysis (TGA) was conducted to evaluate the amount of PEG functionalization on NPs.

Cell cytotoxicity of VLP

RAW 264.7 cells were cultured at 37 °C with 5% CO_2 in Dulbecco's Modified Eagle Medium (DMEM, Biowest), supplemented with 10% fetal bovine serum (FBS, Sigma) and 1% penicillin-streptomycin (Gibco). RAW 264.7 cells were detached with 0.25% Trypsin–EDTA (Gibco) when they reached 80–90% confluence. For the study of cell cytotoxicity, when the confluence of cells reached 80–90%, they were washed with Hanks' balanced salt solution (HBSS, Biowest) three times. And then the cells were added into 96-well plates at a density of 1×10^4 per well and cultured for 24 h, followed by incubation with different concentrations of NPs (50, 100, 200, 400 μg/mL) for 24 h. The positive control is untreated cells, and the negative control was treated with 10% Tween®20. After that, the cells were washed three times with HBSS to remove non-internalized samples. 50 μL fresh cell culture medium was added into the wells, and then 50 μL ATP-based Cell Titer Glo assay (Promega) was added immediately. The plate was incubated at room temperature for 10 minutes, the luminescence was read by Fluoroskan Ascent FL microplate reader (Thermo Labsystems).

Cell uptake of VLP with confocal microscopy *in vitro*

The RAW264.7 cells were seeded in Ibidi 8-well plates with a cell density of 2×10^4 cells per well and incubated for 24 h. The PEG-VLP-NH_2 with varying spike lengths were labeled with Fluorescein 5(6)-isothiocyanate (FITC, Alfa Chemical) for internalization experiments. Specifically, 10 mg of VLPs after modified were stirred with 1 mg FITC in 2 mL of phosphate-buffered saline (PBS, VWR) for 12 hours at room temperature under dark conditions to prevent photodegradation. The FITC-labeled NPs were collected by centrifugation and subsequently washed three times with PBS. And then the different spike length of FITC-labeled VLPs with 50 μg/ml were added into wells and incubated for 4 h. After the incubation, the cells were washed three times with HBSS to remove excess particles before staining with 5μg/mL CellMask™ red plasma membrane for 10 mins in the incubator. Then the cells were washed twice with HBSS and fixed with 4% paraformaldehyde (Sigma-Aldrich) for 10 min at room temperature. For staining nucleus, the cells were stained with 10 μg/ml DAPI (4′,6-diamidino-2-phenylindole, Sigma-Aldrich) for 10 min at room temperature. Finally, the staining solution was replaced with HBSS.

Fluorescence images were captured using a confocal laser scanning microscope instrument (Zeiss LSM 700).

Quantitative proteomics

Raw 264.7 cells were seeded at 6×10^4 cells per well in six-well plates and incubated for 24 hours. Cells were then treated with PEG-VLP-NH_2-0, PEG-VLP-NH_2-5, and PEG-VLP-NH_2-30 NPs (50 μg/mL) for another 12 hours. To prepare Cell Extraction Buffer, Cell Extraction Buffer PTR (ab193970) and Cell Extraction Enhancer Solution (ab193971) were diluted with Milli-Q water and kept on ice. After washing the cells with cold PBS, 200 μL of Cell Extraction buffer was added per well and incubated on ice for 15 minutes. Lysates were centrifuged at 18 000 g for 20 min in a cold condition, and protein content was quantified using the Pierce BCA Protein Assay Kit. Which device did you use to get protein expressions? For all raw data protein expression, the screening criteria for differentially expressed proteins were analyzed by LIMMA test followed by FDR multiple test correction comparing all groups to the control group. Fold change was used to assess alterations in protein expression levels. Student's t-test was performed to calculate p-values, and log2FC cut off was preliminary set at 0.5. The Reactome database system was used to analyze gene-related metabolic pathways by Metascape[18]. In addition, STRING (Search Tool for the Retrieval of Interacting Genes/Proteins) was used to construct a protein-protein interaction network diagram, as described previously[19].

Flow cytometry of VLP

Human PBMC-derived monocyte-derived dendritic cells (MoDCs) were cultured in Roswell Park Memorial Institute (RPMI) medium supplemented with 10% heat-inactivated fetal bovine serum (FBS) (Biowest), 100 U/mL penicillin-streptomycin (Gibco), and 2 mM L-Glutamine (Gibco). Nanoparticles were incubated with the cells for 16 hours. After incubation, the collected cells were resuspended in 100 μL of flow cytometry staining buffer (1× PBS, 10% heat-inactivated FBS [Gibco]) along with the appropriate concentrations of antibodies: HLADR-PE (BioLegend), CD86-PE-Cy7 (BioLegend), CD11c-FITC (BioLegend), CD40-APC (BioLegend), and CD80-BV510 (BD). The cells were incubated for 45 minutes at 4°C in the dark room. After incubation, the samples were washed twice with flow

cytometry running buffer and resuspended in buffer for analysis. Dendritic cells were collected and analyzed using flow cytometry on a NovoCyte Quanteon system (Biomedicum Flow Cytometry Unit). Data analysis was performed using FlowJo V.10.8.1, and graphs were generated using GraphPad Prism 10.3.0.

Statistics and reproducibility

Data are presented as mean ± standard deviation (SD). The significant differences between the two groups were compared using ordinary one-way ANOVA analysis of the means of three or more unmatched groups followed by Dunnett's method was used for multiple comparisons. The p-value is set in figures and legends such as: *$P < 0.05$, **$P < 0.01$, ***$P < 0.001$, ****$P < 0.0001$.

Results and discussion

Physicochemical characterizations

The synthesis of VLP with different spike lengths was performed with the novel single-micelle epitaxial growth approach. The morphology of the VLPs was observed with TEM. The VLP-0 had a spherical shape (Figure 1a) while VLP-5 and VLP-30 presented the virus-like structure with the spike length of 5 and 30 nm (Figure 1b, 1c). The average zeta potential for unmodified VLP-0, VLP-5, and VLP-30 was -24.5, -24.2, and -25.4 mV respectively. After polyethylene glycol (PEG) modification, zeta potential increased to -21.0 mV, -22.0 mV, and -20.5 mV for the PEGylated VLP with 0 nm, 5 nm, and 30 nm spike length, respectively. According to the weight loss in the TGA measurements, the amount of PEG modified on the VLPs was 5.0%, 4.3%, 3.7%, respectively (Figure 1e). After NH_2 modification, surface charge reversed to be positive at +32.6 mV, +29.5 mV and +31.2 mV in the PEG-VLP-NH_2-0, PEG-VLP-NH_2-5, and PEG-VLP-NH_2-30 respectively (Figure 1d).

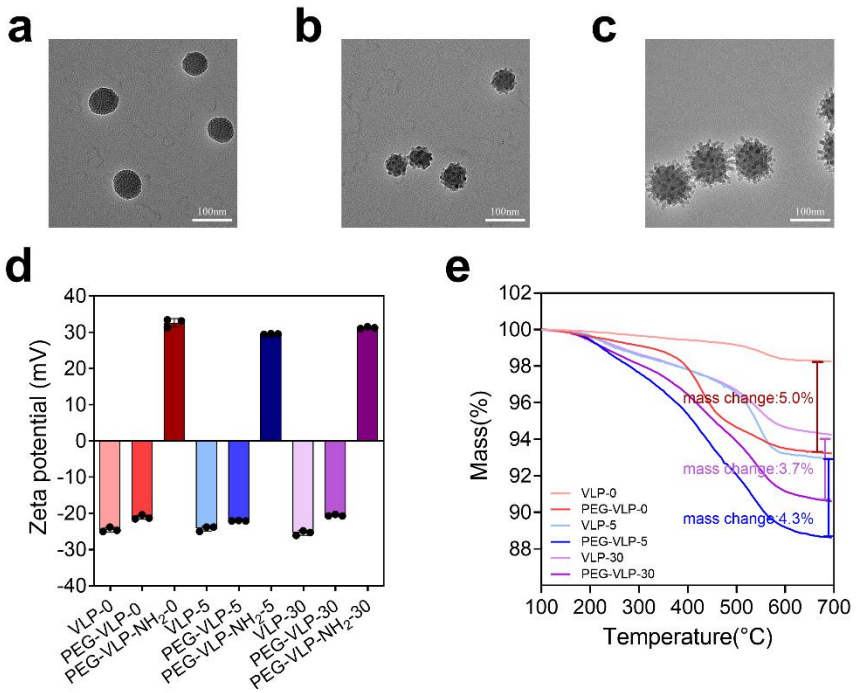

Figure 1. Characterizations of the VLP. (a-c) TEM images of surface morphology of VLP with different spike lengths 0 nm, 5 nm, and 30 nm. Scale bar is 100 nm (d) Zeta potential of VLP before and after surface modifications. (e) Thermogravimetric analysis (TGA) curves of VLPs to quantify PEG amount.

Biocompatibility and cellular uptake of VLP

To investigate the biocompatibility of VLP cell viability of using RAW264.7 cells was measured after incubating the VLPs with four different concentrations (50, 100, 200, 400 μg/mL). The results showed that the unmodified nanoparticles, VLP-0, did not exhibit significant cytotoxicity against RAW264.7 though the concentration was up to 400 μg/mL. However, these VLP-5 and VLi-30 presented cytotoxicity at a concentration of 50 μg/mL reduced cell viability by 23.6% and 25.1%, respectively. When the concentration increased, there was a significant decrease in cell viability. In PEGylated and amine-modified materials, the PEG-VLP-NH_2-0 and PEG-VLP-NH_2-5 did not have any impact on cell viability in the concentration range of 50-400 μg/mL. For PEG-VLP-NH_2-30, 50 μg/mL NPs did not cause cytotoxicity while cell viabilities tend to decrease with the concentration increase of the NPs. 400 μg/mL

PEG-VLP-NH_2-30 decreased the cell viability to 62.1%. These findings indicated that PEGylation can reduce the cytotoxicity of VLP. However, the results also indicated that the VLP with long spikes still have an impact on cell viability with the increase of concentration (Figure 2a).

The cellular uptake efficiency of VLPs largely determined the immune response efficacy of vaccines. Thus, the uptake of VLPs was evaluated by fluorescence images with RAW264.7 cells. As shown in Figure 2b, PEG-VLP-NH_2-30 has the highest cell uptake as compared to PEG-VLP-NH_2-5 and PEG-VLP-NH_2-0. Therefore, the result suggested that the enhancement in cellular uptake efficiency was mainly attributed to biomimetic spiky morphology. Cellular uptake efficiency is much higher when the spike length is longer. This is also explained why PEG-VLP-NH_2-30 showed more cytotoxicity than both PEG-VLP-NH_2-5 and PEG-VLP-NH_2-0 in Figure 2a.

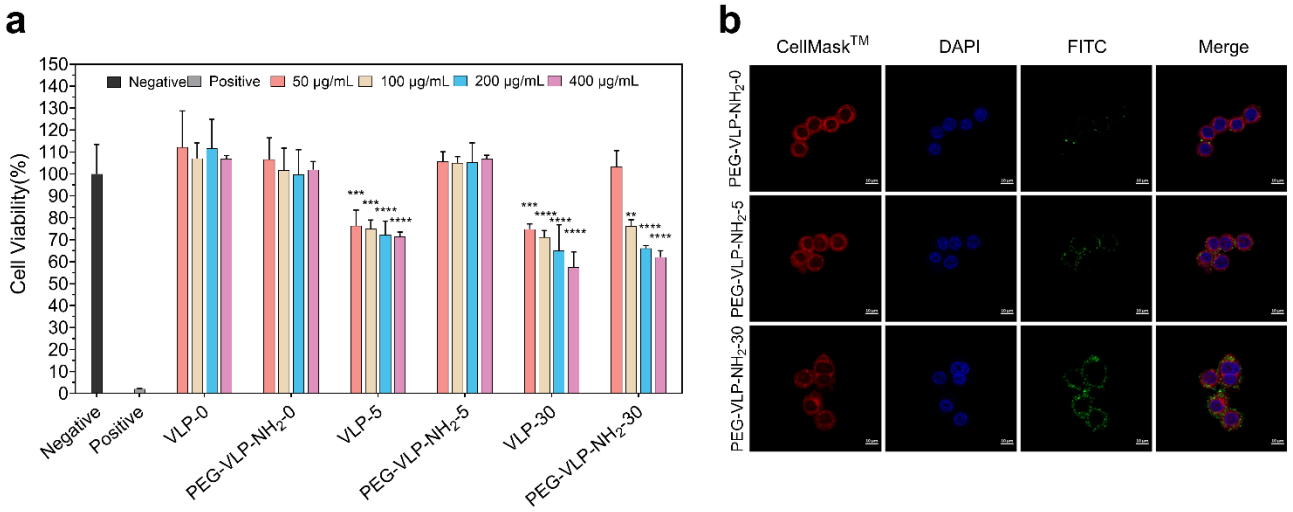

Figure 2. The effect of virus-like mesopores silica nanoparticles on cellular toxicity and uptake of RAW264.7 cells. a) Cell viability of Raw264.7 cells treated with different VLPs after 24h incubation with different concentrations. The data represents mean ± SD. *, **, *** and **** represent statistically significant differences $P < 0.05$, $P < 0.01$, $P < 0.001$ and $P < 0.0001$, respectively. b) Fluorescence images to study cellular uptake of VLPs with different lengths of surface spikes. The VLP labeled with FITC (green color), the nucleus labeled with DAPI (blue color) and cell membrane labeled with CellMask™ (red color). The scale bar is 10μm.

Protein expression of cells treated with VLP

Protein-Protein Interaction Networks were studied using String software to explore the relationship between differentially expressed proteins (Figure 3). In PEG-VLP-NH_2-0, the upregulated protein network consisted of 71 nodes and 45 edges, with an average node degree of 1.27 and a local clustering coefficient of 0.44, forming 15 clusters. The downregulated proteins formed a smaller network with 37 nodes and 21 edges (average node degree: 1.14) and a local clustering coefficient of 0.39, clustering into 5 groups. Compared to PEG-VLP-NH_2-0, PEG-VLP-NH_2-5 exhibited an increase in both network size and connectivity. The upregulated proteins expanded to 79 nodes and 51 edges (average node degree: 1.29) while maintaining the same local clustering coefficient of 0.44, forming 16 clusters. The downregulated network showed an even more pronounced increase in connectivity, with 45 nodes and 52 edges (average node degree: 2.31), a local clustering coefficient of 0.435, and 6 clusters. The most significant expansion occurred in PEG-VLP-NH_2-30, where the upregulated protein network reached 101 nodes and 62 edges, with an average node degree of 1.23 and a slightly lower local clustering coefficient of 0.43, forming 21 clusters. Notably, clusters related to immune pathways were also more visible in the sample of PEG-VLP-NH_2-30. For example, the interaction cluster containing Traf1, Bcl10, and Tab1 which is associated with the TNFR1-induced NF-κB signaling pathway was found. The downregulated network also exhibited substantial growth, increasing to 65 nodes and 90 edges, with an average node degree of 2.77 and a higher local clustering coefficient of 0.49, forming 8 clusters. Overall, the results suggested the protein interaction networks varied across PEG-VLP-NH_2-0, PEG-VLP-NH_2-5, and PEG-VLP-NH_2-30, showing progressive increases in node count, connectivity, and clustering complexity while increasing spike length.

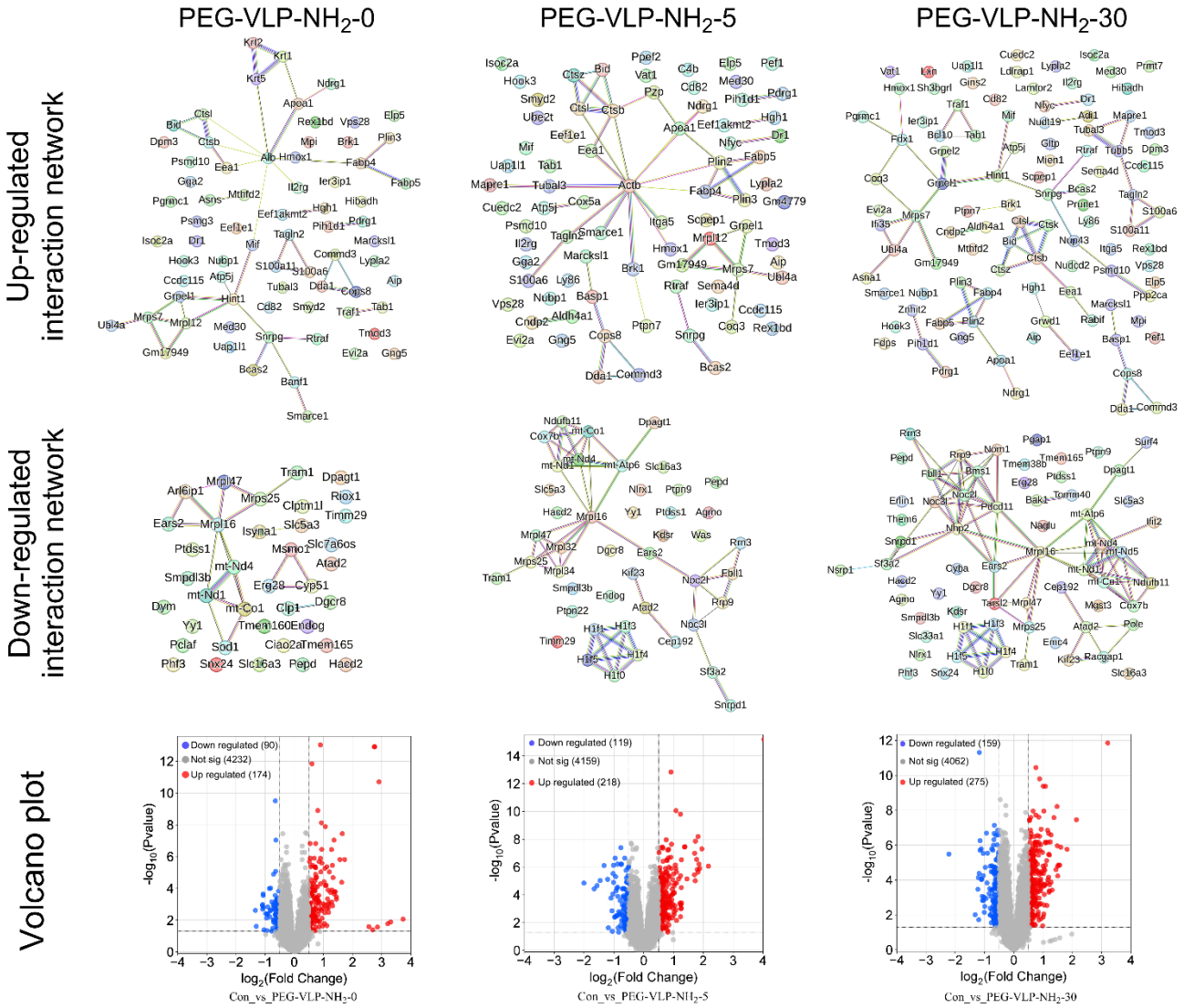

Figure 3. The differentially expressed proteins from PEG-VLP-NH_2 compared with control. STRING Protein-Protein Interaction Networks of PEG-VLP-NH_2-0, PEG-VLP-NH_2-5, and PEG-VLP-NH_2-30 with upregulated expressed protein, and down regulated expressed protein. Volcano plot of expressed proteins from VLP with different spike lengths compared with control. The red dots represent the upregulated proteins, the blue dots represent the downregulated proteins, and the gray dots represent no significant change ($P < 0.05$, $|\log2FC|>0.5$).

Pathways of immune response activated by VLP

Functional enrichment analysis was performed to study the pathways involved in the activation of immune cells by using Metascape with Reactome database. The most significant enriched pathways of different samples are shown in Figure 4. In PEG-VLP-NH_2-0, upregulated keratinization and formation of the cornified envelope show high enrichment while no significant immune-related pathways were identified (Figure 4a). Pathways related to G alpha (s) signaling events are significantly enriched in the upregulated proteins of PEG-VLP-NH_2-5 (Figure 4b). The G alpha (s) signaling events pathway is related to the activation of G protein-coupled receptors (GPCRs). When activated, it in turn stimulates adenylate cyclase to produce cyclic AMP (cAMP), consequently triggering various cellular signal transduction [20].

The upregulated proteins in PEG-VLP-NH_2-30, trafficking and processing of endosomal Toll-like Receptor (TLR), TLR Cascades, and NF-kappa B signaling pathway are significantly enriched (Figure 4c). TLRs activate a common signaling pathway, ultimately leading to the activation of the nuclear factor κB (NF-κB) transcription factor, as well as mitogen-activated protein kinases (MAPKs), including extracellular signal-regulated kinase (ERK), p38, and c-Jun N-terminal kinase (JNK). This cascade subsequently promotes the transcription of pro-inflammatory cytokines[21,22]. The down regulated protein for pathway enrichment analysis was shown in Figure S2, it doesn't have the pathways related to immune that we are interested in. The all heatmap results highlight the expressed proteins in these functional pathways after the treatments with VLP of varying spike lengths. The level of differential expression was quantified by logFC. Differential expressions of proteins involved RIG-I-like receptors, chemokine, MAPK, TLR signaling pathways and Th1 and Th2 cell differentiation (Figure 4d, S3). It is shown that the spike length can stimulate the protein expression in the signaling pathways.

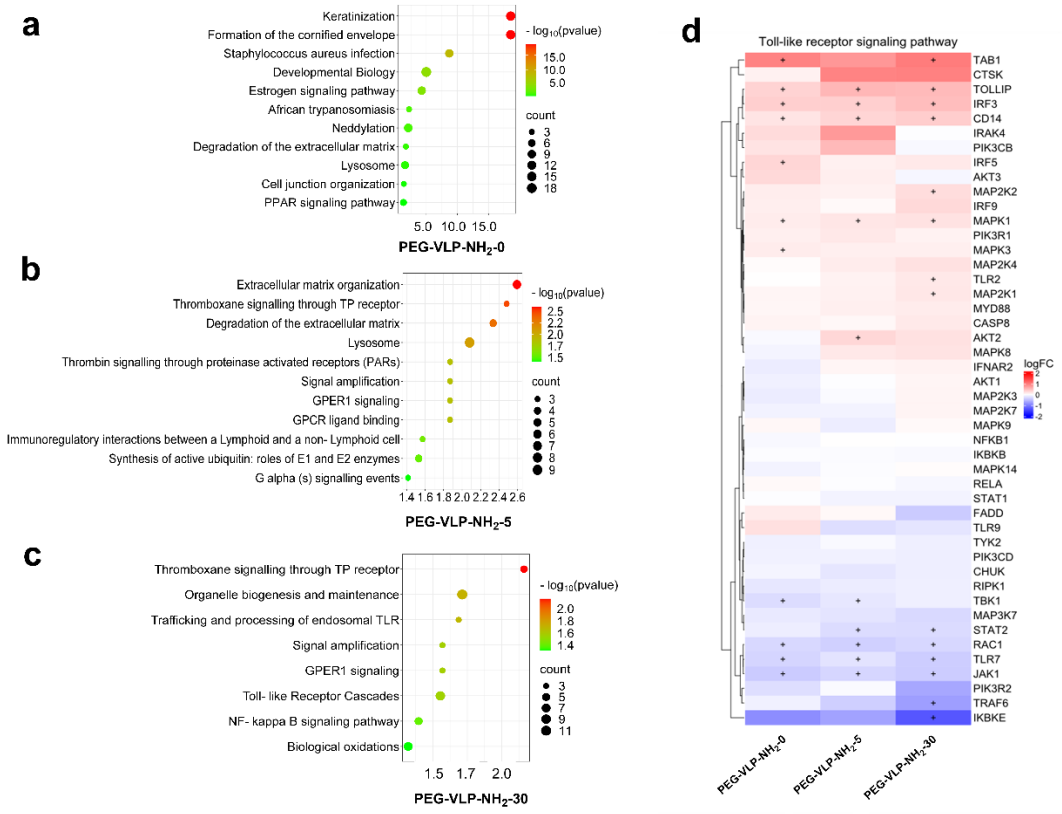

Figure 4. Pathway analysis after the cells incubated with three nanoparticles. a. Pathway enrichment analysis of up-regulated proteins from Reactome database, a. PEG-VLP-NH_2-0. b. PEG-VLP-NH_2-5. c. PEG-VLP-NH_2-30. Statistically significant enriched pathways are shown, the size of the dot reflects the count of proteins involved in that pathway, and the color scale indicates the statistical significance (-log10 (p-value)). d. Toll-like receptor signaling pathway heatmap from an Immunological database. + represents the p-value is lower than 0.01.

The candidate proteins analysis in immune response

The heatmap was generated to show the relevance between three spike lengths of nanomaterial and protein expression levels. It is important to study the mechanisms when the spiky length are increasing, focusing on proteins related to immune responses, such as TRAF6, and PIAS4 (Figure 5a). while some proteins get changed with spiky length decreasing (Figure 5b). Among these, TRAF6, a member of the tumor necrosis factor receptor-associated factor (TRAF) family of adaptor proteins, is a RING domain-containing E3 ubiquitin ligase (Figure 5c). It plays a key role in different signaling pathways and

biological processes, serving as an important target for pro-inflammatory and immunoregulatory factors. Additionally, TRAF6 significantly enhances the transcriptional activation of nuclear factor κB (NF-κB), thereby playing an important role in the activation of innate immune responses[23].TRAF6 is involved in multiple signaling pathways, and the Toll-like receptor 4 (TLR4) signaling pathway being particularly noteworthy. This pathway includes both MyD88-dependent and MyD88-independent mechanisms[24], which subsequently cause a cascade of events leading to the activation of the MAPK pathway[25], hereby cause immune-related responses. And PIAS4 (Figure 5d), a protein inhibitor of activated STAT4, plays a crucial role as a transcriptional coregulator in various cellular pathways. For example, PIAS4 may promote NF-κB activation by SUMOylating the inhibitor of NF-κB kinase subunit gamma (IKBKG)[26], and then affect the immune response.

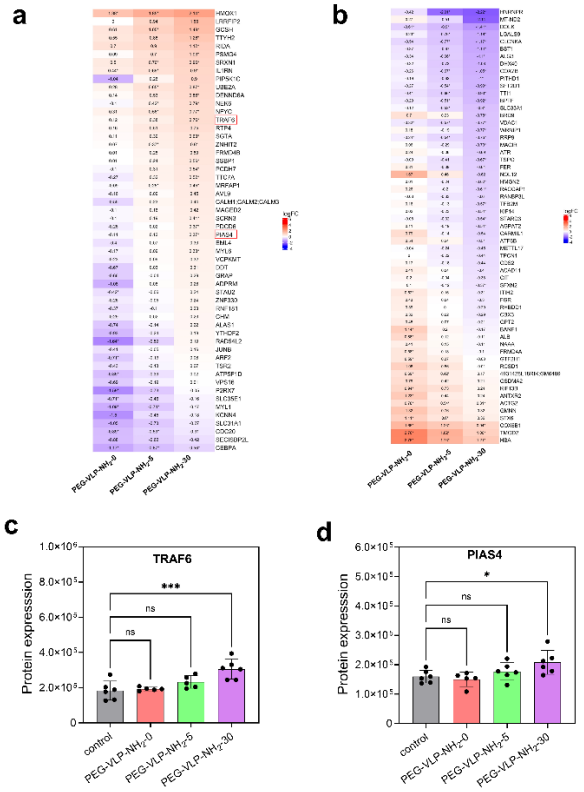

Figure 5. Heatmap about nanoparticle length-dependent protein regulation. a. The protein expression increased with the nanoparticle spiky length compared to the control. b. The protein expression decreased with nanoparticle spiky length. Protein expressions are shown as log2FC, red and blue colors correspond to significantly up-regulated proteins

compared to the control. The difference between each group is log2FC = 0.5 and the p-value is marked when lower than 0.05, The significant protein expressions from proteomics analysis. c. TRAF6, d. PIAS4, *, **, ***and **** represent statistically significant differences $P < 0.05$, $P < 0.01$, $P < 0.001$ and $P < 0.0001$, respectively

Activation of immune response *in vitro*

Various surface markers on immune cells, such as CD80, CD86, CD40, CD11c, and HLA-DR, are essential for T cell activation and immune regulation. The surface expression of these immune-related markers was studied with flow cytometry. The expressions of CD86 and CD80 were significantly upregulated in the PEG-VLP-NH_2-30 as compared to the PEG-VLP-NH_2-0 and PEG-VLP-NH_2-5, indicating an excellent ability of long-spiky VLP in activation of DCs (Figure 6a, 6b). CD80 and CD86 are co-stimulatory molecules for T cell activation and proliferation[27]. They are also markers for M1 macrophage activation[28]. The CD28/CD80 co-stimulatory signal activates pathways such as NF-kappa-B and MAPK, leading to the production of cytokines that initiate immune responses[29]. CD86 interacts with its ligands, CD28 or CTLA-4, to induce T lymphocyte proliferation and IL-2 production and is also involved in regulating B cell function[30,31]. HLA-DR, an MHC class II molecule, presents antigens to $CD4^+$ T helper cells and is essential for initiating adaptive immune responses[32]. HLA-DR expression was significantly increased ($p < 0.001$) in the PEG-VLP-NH_2-5 and PEG-VLP-NH_2-30 as compared to the PEG-VLP-NH2-0 (Figure 6c). Furthermore, HLA-DR expression was enhanced with an increasing spike length (Figure 6d). The VLP did not lead to a significant change in the expression of CD11c and CD40 regardless of spike length (Figure S4). These results suggested the VLPs have the potential to enhance antigen presentation to $CD4^+$ T helper cells for cancer immunotherapy. Taking together, we can conclude that VLPs are effective to activate immune response, and their spike length plays a critical role in controlling efficacy of immune stimulation.

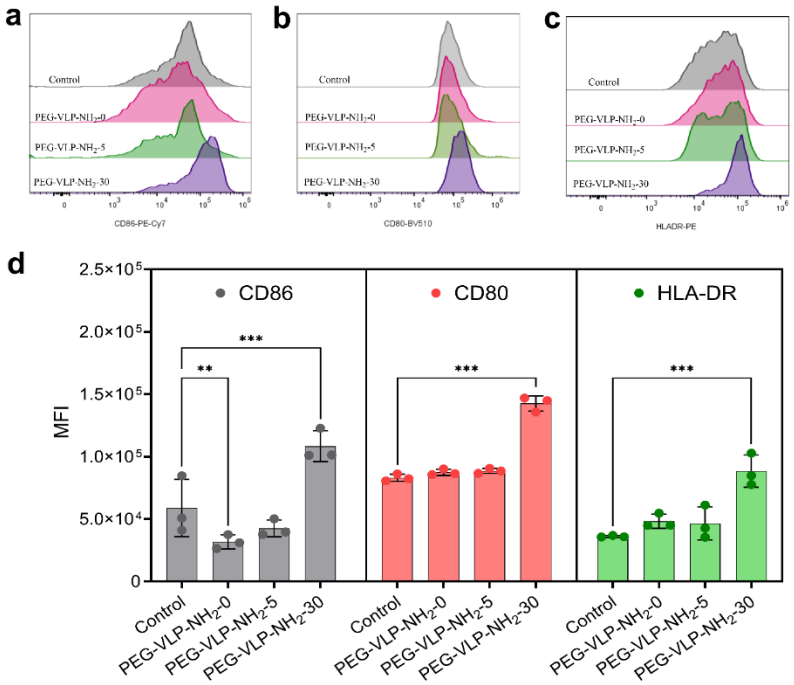

Figure 6. Flow cytometry analysis about CD80, CD86, and HLA-DR on human PBMC monocyte-derived dendritic cells (MoDCs) after being incubated with 50 μg/mL PEG-VLP-NH_2-0, PEG-VLP-NH_2-5, and PEG-VLP-NH_2-30. a. CD86. b. CD80. c. HLA-DR. d. The violin plots quantify the expression levels. *, **, and *** indicate statistically significant differences with $P < 0.05$, $P < 0.01$, and $P < 0.001$, respectively.

Conclusions

In this study, we investigated the effects of different spike lengths on immune response. Compared to smooth mesoporous silica particles, our findings showed that particles with longer spikes (30 nm) showed higher cellular uptake efficiency. Proteomic analysis indicated that longer spikes induced more differentially expressed proteins. The RIG-I-like receptors, chemokine, MAPK, Toll-like receptor signaling pathways, and Th1and Th2 cell differentiation pathways were involved in regulating the immune response. The expression levels of TRAF6 and PIAS4 proteins changed with spike length, impacting immune responses. Furthermore, we verified the VLP could effectively deliver antigens to $CD4^+$T cells and stimulate immune response by upregulating CD86, CD80, and HLA-DR expression.

The present study may reveal novel targets for utilizing biomimetic virus-like nanomaterials as immunoadjuvants to enhance immunotherapy.

Acknowledgments

This work was carried out with financial support from Research Council of Finland (Grant no. 356056, 359706, and 356992), program of China Scholarship Council, and Cancer Foundation Finland. SIB Labs, UEF Cell and the Tissue Imaging Unit were acknowledged for technical support.

Declaration of Competing Interest

The authors declare that they have no known competing financial interests or personal relationships that could have appeared to influence the work reported in this article.

Reference

(1) Xu, B.; Li, S.; Shi, R.; Liu, H. Multifunctional Mesoporous Silica Nanoparticles for Biomedical Applications. *Sig Transduct Target Ther* **2023**, *8* (1), 435. https://doi.org/10.1038/s41392-023-01654-7.

(2) Wen, H.; Tamarov, K.; Happonen, E.; Lehto, V.; Xu, W. Inorganic Nanomaterials for Photothermal-Based Cancer Theranostics. *Advanced Therapeutics* **2021**, *4* (2), 2000207. https://doi.org/10.1002/adtp.202000207.

(3) Mody, K. T.; Popat, A.; Mahony, D.; Cavallaro, A. S.; Yu, C.; Mitter, N. Mesoporous Silica Nanoparticles as Antigen Carriers and Adjuvants for Vaccine Delivery. *Nanoscale* **2013**, *5* (12), 5167. https://doi.org/10.1039/c3nr00357d.

(4) Yu, A.; Dai, X.; Wang, Z.; Chen, H.; Guo, B.; Huang, L. Recent Advances of Mesoporous Silica as a Platform for Cancer Immunotherapy. *Biosensors* **2022**, *12* (2), 109. https://doi.org/10.3390/bios12020109.

(5) Wagner, J.; Gößl, D.; Ustyanovska, N.; Xiong, M.; Hauser, D.; Zhuzhgova, O.; Hočevar, S.; Taskoparan, B.; Poller, L.; Datz, S.; Engelke, H.; Daali, Y.; Bein, T.; Bourquin, C. Mesoporous Silica Nanoparticles as pHResponsive Carrier for the Immune-Activating Drug Resiquimod Enhance the Local Immune Response in Mice. *ACS Nano* **2021**, *15* (3), 4450–4466. https://doi.org/10.1021/acsnano.0c08384.

(6) Escriche-Navarro, B.; Escudero, A.; Lucena-Sánchez, E.; Sancenón, F.; García-Fernández, A.; Martínez-Máñez, R. Mesoporous Silica Materials as an Emerging Tool for Cancer Immunotherapy. *Advanced Science* **2022**, *9* (26), 2200756. https://doi.org/10.1002/advs.202200756.

(7) Zhang, R.; Qin, X.; Kong, F.; Chen, P.; Pan, G. Improving Cellular Uptake of Therapeutic Entities through Interaction with Components of Cell Membrane. *Drug Delivery* **2019**, *26* (1), 328–342. https://doi.org/10.1080/10717544.2019.1582730.

(8) Sougrat, R.; Bartesaghi, A.; Lifson, J. D.; Bennett, A. E.; Bess, J. W.; Zabransky, D. J.; Subramaniam, S. Electron Tomography of the Contact between T Cells and SIV/HIV-1: Implications for Viral Entry. *PLoS Pathog* **2007**, *3* (5), e63. https://doi.org/10.1371/journal.ppat.0030063.

(9) Chen, H.-J.; Hang, T.; Yang, C.; Liu, D.; Su, C.; Xiao, S.; Liu, C.; Lin, D.; Zhang, T.; Jin, Q.; Tao, J.; Wu, M. X.; Wang, J.; Xie, X. Functionalized Spiky Particles for Intracellular Biomolecular Delivery. *ACS Cent. Sci.* **2019**, *5* (6), 960–969. https://doi.org/10.1021/acscentsci.8b00749.

(10) Xu, C.; Niu, Y.; Popat, A.; Jambhrunkar, S.; Karmakar, S.; Yu, C. Rod-like Mesoporous Silica Nanoparticles with Rough Surfaces for Enhanced Cellular Delivery. *J. Mater. Chem. B* **2014**, *2* (3), 253–256. https://doi.org/10.1039/C3TB21431A.

(11) Häffner, S. M.; Parra-Ortiz, E.; Browning, K. L.; Jørgensen, E.; Skoda, M. W. A.; Montis, C.; Li, X.; Berti, D.; Zhao, D.; Malmsten, M. Membrane Interactions of Virus-like Mesoporous Silica Nanoparticles. *ACS Nano* **2021**, *15* (4), 6787–6800. https://doi.org/10.1021/acsnano.0c10378.

(12) Wang, W.; Wang, P.; Tang, X.; Elzatahry, A. A.; Wang, S.; Al-Dahyan, D.; Zhao, M.; Yao, C.; Hung, C.-T.; Zhu, X.; Zhao, T.; Li, X.; Zhang, F.; Zhao, D. Facile Synthesis of Uniform Virus-like Mesoporous Silica Nanoparticles for Enhanced Cellular Internalization. *ACS Cent. Sci.* **2017**, *3* (8), 839–846. https://doi.org/10.1021/acscentsci.7b00257.

(13) Gao, Y.; Zhang, Y.; Xia, H.; Ren, Y.; Zhang, H.; Huang, S.; Li, M.; Wang, Y.; Li, H.; Liu, H. Biomimetic Virus-like Mesoporous Silica Nanoparticles Improved Cellular Internalization for Co-Delivery of Antigen and Agonist to Enhance Tumor Immunotherapy. *Drug Delivery* **2023**, *30* (1), 2183814. https://doi.org/10.1080/10717544.2023.2183814.

(14) Abdelkader, Y.; Perez-Davalos, L.; LeDuc, R.; Zahedi, R. P.; Labouta, H. I. Omics Approaches for the Assessment of Biological Responses to Nanoparticles. *Advanced Drug Delivery Reviews* **2023**, *200*, 114992. https://doi.org/10.1016/j.addr.2023.114992.

(15) Tenzer, S.; Docter, D.; Rosfa, S.; Wlodarski, A.; Kuharev, J.; Rekik, A.; Knauer, S. K.; Bantz, C.; Nawroth, T.; Bier, C.; Sirirattanapan, J.; Mann, W.; Treuel, L.; Zellner, R.; Maskos, M.; Schild, H.; Stauber, R. H. Nanoparticle Size Is a Critical Physicochemical Determinant of the Human Blood Plasma Corona: A Comprehensive Quantitative Proteomic Analysis. *ACS Nano* **2011**, *5* (9), 7155–7167. https://doi.org/10.1021/nn201950e.

(16) Elechalawar, C. K.; Hossen, Md. N.; McNally, L.; Bhattacharya, R.; Mukherjee, P. Analysing the Nanoparticle-Protein Corona for Potential Molecular Target Identification. *Journal of Controlled Release* **2020**, *322*, 122–136. https://doi.org/10.1016/j.jconrel.2020.03.008.

(17) Collin-Faure, V.; Dalzon, B.; Devcic, J.; Diemer, H.; Cianférani, S.; Rabilloud, T. Does Size Matter? A Proteomics-Informed Comparison of the Effects of Polystyrene Beads of Different Sizes on Macrophages. *Environ. Sci.: Nano* **2022**, *9* (8), 2827–2840. https://doi.org/10.1039/D2EN00214K.

(18) Zhou, Y.; Zhou, B.; Pache, L.; Chang, M.; Khodabakhshi, A. H.; Tanaseichuk, O.; Benner, C.; Chanda, S. K. Metascape Provides a Biologist-Oriented Resource for the Analysis of Systems-Level Datasets. *Nat Commun* **2019**, *10* (1), 1523. https://doi.org/10.1038/s41467-019-09234-6.

(19) Hussein, H.; Kishen, A. Proteomic Profiling Reveals Engineered Chitosan Nanoparticles Mediated Cellular Crosstalk and Immunomodulation for Therapeutic Application in Apical Periodontitis. *Bioactive Materials* **2022**, *11*, 77–89. https://doi.org/10.1016/j.bioactmat.2021.09.032.

(20) Kehrl, J. H. Heterotrimeric G Protein Signaling: Roles in Immune Function and Fine-Tuning by RGS Proteins. *Immunity* **1998**, *8* (1), 1–10. https://doi.org/10.1016/S1074-7613(00)80453-7.

(21) Barton, G. M.; Medzhitov, R. Toll-Like Receptor Signaling Pathways. *Science* **2003**, *300* (5625), 1524–1525. https://doi.org/10.1126/science.1085536.

(22) Kawai, T.; Ikegawa, M.; Ori, D.; Akira, S. Decoding Toll-like Receptors: Recent Insights and Perspectives in Innate Immunity. *Immunity* **2024**, *57* (4), 649–673. https://doi.org/10.1016/j.immuni.2024.03.004.

(23) Bidère, N.; Snow, A. L.; Sakai, K.; Zheng, L.; Lenardo, M. J. Caspase-8 Regulation by Direct Interaction with TRAF6 in T Cell Receptor-Induced NF-κB Activation. *Current Biology* **2006**, *16* (16), 1666–1671. https://doi.org/10.1016/j.cub.2006.06.062.

(24) Kawai, T.; Akira, S. The Role of Pattern-Recognition Receptors in Innate Immunity: Update on Toll-like Receptors. *Nat Immunol* **2010**, *11* (5), 373–384. https://doi.org/10.1038/ni.1863.

(25) Li, J.; Liu, N.; Tang, L.; Yan, B.; Chen, X.; Zhang, J.; Peng, C. The Relationship between TRAF6 and Tumors. *Cancer Cell Int* **2020**, *20* (1), 429. https://doi.org/10.1186/s12935-020-01517-z.

(26) Mabb, A. M.; Wuerzberger-Davis, S. M.; Miyamoto, S. PIASy Mediates NEMO Sumoylation and NF-κB Activation in Response to Genotoxic Stress. *Nat Cell Biol* **2006**, *8* (9), 986–993. https://doi.org/10.1038/ncb1458.

(27) Sansom, D. M.; Manzotti, C. N.; Zheng, Y. What's the Difference between CD80 and CD86? *Trends in Immunology* **2003**, *24* (6), 313–318. https://doi.org/10.1016/S1471-4906(03)00111-X.

(28) Ishizuka, E. K.; Ferreira, M. J.; Grund, L. Z.; Coutinho, E. M. M.; Komegae, E. N.; Cassado, A. A.; Bortoluci, K. R.; Lopes-Ferreira, M.; Lima, C. Role of Interplay between IL-4 and IFN-γ in the in Regulating M1 Macrophage Polarization Induced by Nattectin. *International Immunopharmacology* **2012**, *14* (4), 513–522. https://doi.org/10.1016/j.intimp.2012.08.009.

(29) Boulougouris, G.; McLeod, J. D.; Patel, Y. I.; Ellwood, C. N.; Walker, L. S. K.; Sansom, D. M. IL-2-Independent Activation and Proliferation in Human T Cells Induced by CD28. *The Journal of Immunology* **1999**, *163* (4), 1809–1816. https://doi.org/10.4049/jimmunol.163.4.1809.

(30) Collins, A. V.; Brodie, D. W.; Gilbert, R. J. C.; Iaboni, A.; Manso-Sancho, R.; Walse, B.; Stuart, D. I.; Van Der Merwe, P. A.; Davis, S. J. The Interaction Properties of Costimulatory Molecules Revisited. *Immunity* **2002**, *17* (2), 201–210. https://doi.org/10.1016/S1074-7613(02)00362-X.

(31) Lanier, L. L.; O'Fallon, S.; Somoza, C.; Phillips, J. H.; Linsley, P. S.; Okumura, K.; Ito, D.; Azuma, M. CD80 (B7) and CD86 (B70) Provide Similar Costimulatory Signals for T Cell Proliferation, Cytokine Production, and Generation of CTL. *The Journal of Immunology* **1995**, *154* (1), 97–105. https://doi.org/10.4049/jimmunol.154.1.97.

(32) Gay, D.; Maddon, P.; Sekaly, R.; Talle, M. A.; Godfrey, M.; Long, E.; Goldstein, G.; Chess, L.; Axel, R.; Kappler, J.; Marrack, P. Functional Interaction between Human T-Cell Protein CD4 and the Major Histocompatibility Complex HLA-DR Antigen. *Nature* **1987**, *328* (6131), 626–629. https://doi.org/10.1038/328626a0.